ARTICLES
PUBLISHED ONLINE: 18 SEPTEMBER 2017 | DOI: 10.1038/NMAT4975
nature materials

Resolving ultrafast exciton migration in organic solids at the nanoscale

Samuel B. Penwell[1†], Lucas D. S. Ginsberg[1], Rodrigo Noriega[1†] and Naomi S. Ginsberg[1,2,3,4,5★]

Effectiveness of molecular-based light harvesting relies on transport of excitons to charge-transfer sites. Measuring exciton migration, however, has been challenging because of the mismatch between nanoscale migration lengths and the diffraction limit. Instead of using bulk substrate quenching methods, here we define quenching boundaries all-optically with sub-diffraction resolution, thus characterizing spatiotemporal exciton migration on its native nanometre and picosecond scales. By transforming stimulated emission depletion microscopy into a time-resolved ultrafast approach, we measure a 16-nm migration length in poly(2,5-di(hexyloxy)cyanoterephthalylidene) conjugated polymer films. Combined with Monte Carlo exciton hopping simulations, we show that migration in these films is essentially diffusive because intrinsic chromophore energetic disorder is comparable to chromophore inhomogeneous broadening. Our approach will enable previously unattainable correlation of local material structure to exciton migration character, applicable not only to photovoltaic or display-destined organic semiconductors but also to explaining the quintessential exciton migration exhibited in photosynthesis.

Complex materials with electronically coupled chromophores, such as those in organic or composite nanocrystal photovoltaics and light-emitting diodes, or in photosynthetic light harvesting, rely on the migration of tightly bound, localized, short-lived excitons for energy transduction[1–9]. Exciton migration in photosynthesis is nearly 100% efficient, but the design principles enabling efficient transport in such complex and disordered systems have remained challenging[7,8]. Conversely, organic photovoltaic performance has been limited by the short, ∼5–20-nm range of exciton migration in organic semiconductors[4,6,10–15]. There has been considerable effort to understand the origin of these limited migration lengths, but the development of a complete physical picture of the migration process has been hindered by the challenge associated with measuring exciton migration and correlating it to the local, disordered material substructure[16–21]. Since excitons are optical excitations, spatial resolution in migration measurements is generally limited by diffraction to >200 nm, even though migration lengths are one to two orders of magnitude smaller. Typically, this challenge is addressed by depositing a set of thin films with thicknesses of the order of the migration length onto exciton-quenching substrates. The length scale of exciton migration is then estimated from the dependence of the resulting photoluminescence quenching on film thickness[4,10,14,15]. These measurements, however, do not necessarily represent exciton migration in the absence of the quenching layer, and are limited in their ability to discern heterogeneity since they average over areas larger than the scales of heterogeneity and require measuring multiple sample preparations[4,10,22]. Recently, an elegant new method was demonstrated that removes the need for a quenching boundary by resolving, over the nanoseconds timescale of fluorescence decay, the very small expansion of an excitation volume prepared at the diffraction limit[23,24]. Here we present an approach to surmount both the diffraction limit and the need for a physical quenching layer by employing an optical quenching boundary. Surmounting the diffraction limit leads to probe volumes with larger perimeter-to-area ratios so that migration near the perimeter forms a larger fraction of our signal and should also enable investigation of exciton migration heterogeneity on the scales of physical heterogeneity.

Measuring exciton migration

We have measured exciton migration in organic semiconducting conjugated polymer films on its native nanometre and picosecond scales. We did so by producing an ultrafast optical exciton-quenching boundary, defined through spatially varying light–matter interactions on the characteristic scales of migration. More specifically, this feat first required that we extend photophysically restrictive stimulated emission depletion (STED) microscopy to electronically coupled materials with endogenous chromophores[25]. It furthermore required that we devise a means to use the sharp, sub-diffraction excited-state population profile thus created to both induce and measure the spatiotemporal evolution of the exciton distribution. STED microscopy is a form of super-resolution fluorescence imaging in which a pump laser pulse creates a diffraction-limited excitation distribution, and a depletion laser pulse, with an annular transverse mode, drives stimulated emission around the periphery of the excitation distribution[26]. Only the small fraction of excitations at the centre of the original distribution survives, defining a sub-diffraction excitation volume that can in principle be vanishingly small due to the intensity-dependent depletion saturation of the sample. As shown in our time-resolved ultrafast STED (TRUSTED) scheme in Fig. 1a frames 1 and 2, we use this combination of a pump and an annular depletion pulse to define a sub-diffraction excitation volume of <100 nm (Supplementary Fig. 1), but it is only able to serve as an initial condition for migration. Tracking the nanoscale exciton redistribution over its very brief lifetime requires additional innovation because emitted

[1]Department of Chemistry, University of California, Berkeley, California 94720, USA. [2]Molecular Biophysics and Integrated Bioimaging Division, Lawrence Berkeley National Laboratory, Berkeley, California 94720, USA. [3]Materials Science Division, Lawrence Berkeley National Laboratory, Berkeley, California 94720, USA. [4]Kavli Energy NanoScience Institute, Berkeley, California 94720, USA. [5]Department of Physics, University of California, Berkeley, California 94720, USA. †Present addresses: James Franck Institute, University of Chicago, Chicago, Illinois 60637, USA (S.B.P.); Department of Chemistry, University of Utah, Salt Lake City, Utah 84112, USA (R.N.). ★e-mail: nsginsberg@berkeley.edu

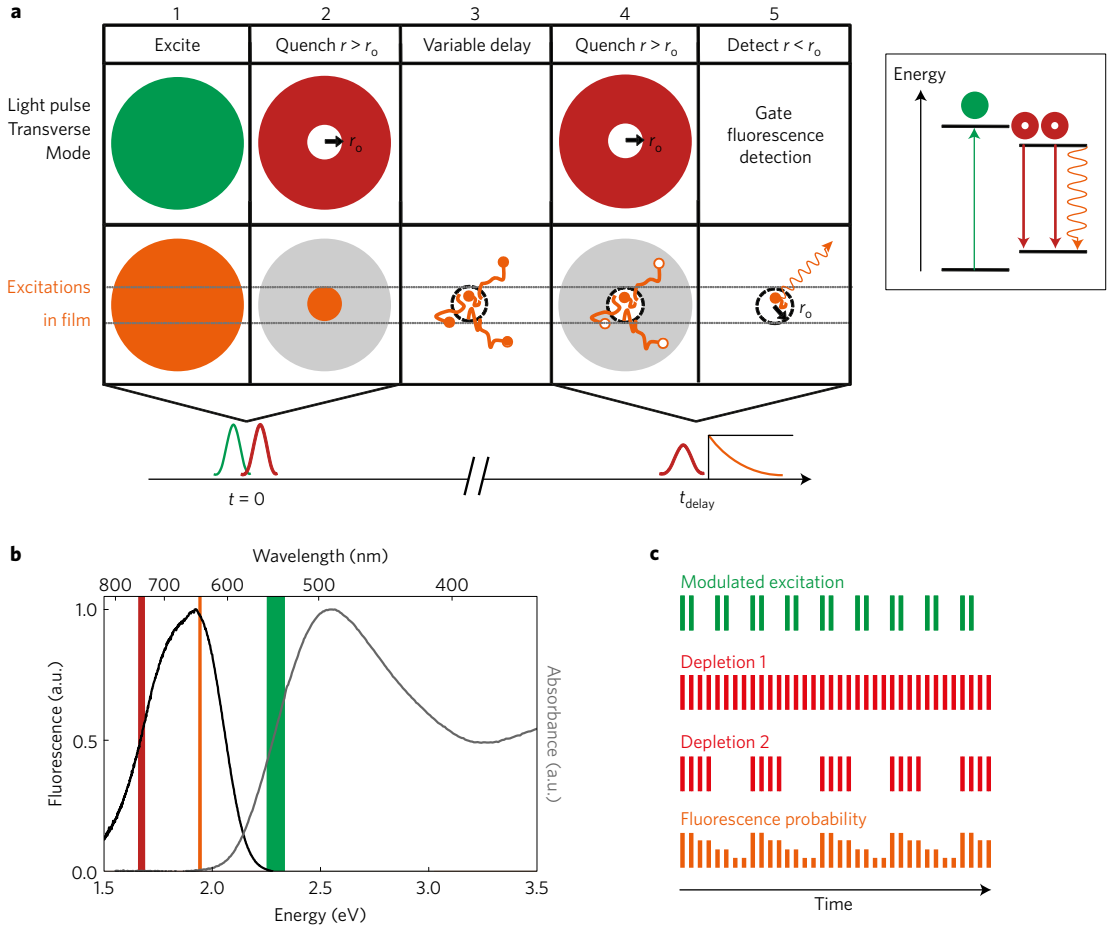

Figure 1 | TRUSTED implementation. a, TRUSTED sequence schematic showing the process in space, energy and time. **b**, Absorbance and fluorescence spectra of CN-PPV solids. Coloured bands indicate the location and width of the pump pulse (green), depletion pulse (red), and fluorescence detection window (orange). **c**, Sketch of modulation scheme employed. Only a few pulses are shown per on/off phase although the 200-kHz pulse repetition rate far exceeds the mechanical modulation frequencies.

light collected in the far field does not encode information about the specific location (or spatial distribution) of emission and its evolution from the initial excitation profile.

We respond to this challenge by following the preparation of the excitation volume with a second annular depletion pulse. This pulse defines a subsequent sub-diffraction detection volume that produces a coaxial quenching boundary at a controllable and variable time delay (Fig. 1a frame 4). The sharply confined sub-diffraction excitation volume initially has steep gradients at its boundary, inducing larger subsequent relative changes to the distribution than are achievable otherwise. By using the second depletion pulse to redefine a quenching boundary identical to the initial one, excitons that migrate beyond this boundary in the intervening period may be quenched. The extent of migration over time can thus be resolved by progressively increasing this intervening migration period over successive measurements and collecting fluorescence emission only from the correspondingly decreasing population remaining in the resulting 'detection volume' at the instant this second depletion pulse is applied (Fig. 1a frame 5). The length scale and timescale of migration are encoded in the decay of the observed fluorescence signal as a function of this delay time. This TRUSTED approach enables us to measure migration on its native spatial and temporal scales in the absence of a physical quenching boundary, thereby opening the possibility for correlative measurements with the local material morphology to develop an understanding of the structure/function relationship that governs exciton migration.

We employ the TRUSTED scheme on poly(2,5-di(hexyloxy) cyanoterephthalylidene) (CN-PPV) thin films in a home-built confocal microscope (Supplementary Fig. 2 and Supplementary Text), using a 3-fJ, few-ps pump pulse at 540 nm and two identical 240-pJ, ~120-ps depletion pulses at 740 nm (point spread functions shown in Supplementary Fig. 3). The film has a 5-ns fluorescence lifetime[25,27], τ, and representative absorption and emission spectra are shown in Fig. 1b. We collect fluorescence between 635 and 640 nm and scan the delay time between excitation and detection from 240 ps to 3 ns. Care is taken to avoid sample heating by using transverse rastering. Isolating the component of the measured fluorescence decay that is due to migration requires great care. To do so, we first modulate the 540-nm excitation to eliminate the contribution of any two-photon absorption (2PA) of the depletion pulses to the detected migration signal (see Supplementary Fig. 4 and accompanying text for details)[25]. Second, fluorescence detection using a single-photon counting avalanche photodiode (SPAD) is gated on within <200 ps (ref. 28) approximately 500 ps after the arrival of the second depletion pulse to reject any fluorescence emitted prior to the definition of the detection volume[29]. Last, we normalize the fluorescence signal to that obtained in the absence of the second depletion pulse. This normalization removes the contribution to the decaying signal due to fluorescence decay of excitations and isolates the contribution due to the outflux of excitons from the initially excited volume. (See Fig. 1c for the modulation scheme, Supplementary Table 1 and Supplementary Fig. 5 and accompanying text for details.) The resulting normalized detection volume fluorescence

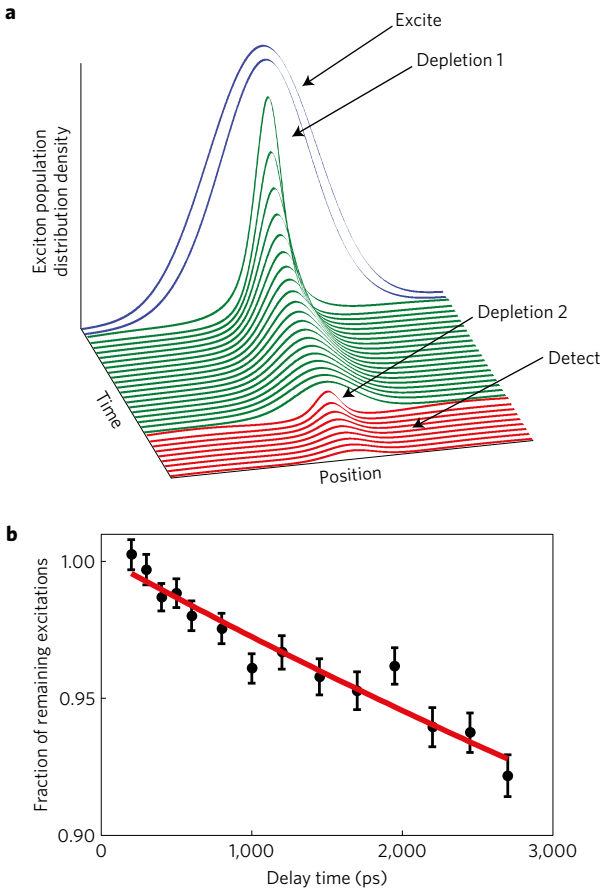

Figure 2 | Using TRUSTED to capture the fraction of remaining excitations versus time to obtain L_d. a, Illustration of the sequence of events and evolution of the model used to fit TRUSTED data. The model includes the diffusive expansion of the initial exciton distribution, subject to the spatially varying depletion pulses. See Supplementary Fig. 6 for full explanation. **b**, Measured fraction of remaining excitation as a function of the delay time defining sub-diffraction excitation and detection volumes in the TRUSTED measurement. See Supplementary Fig. 5 for raw data. Error bars are s.e.m. Red curve indicates a fit of the data to an exciton migration model to yield $L_d = 16 \pm 2$ nm.

can be directly related to the fraction of the exciton population at a given time that survives the definition of the detection volume. Its decay can be attributed to the increase in the fraction of the population that crosses and is quenched beyond the relatively abrupt 'boundary' of this volume as a function of delay time, as simulated in Fig. 2a. The observed fraction of remaining excitons versus delay time for a representative CN-PPV thin film is shown in Fig. 2b. The curve overlaying the data is a fit that assumes diffusive exciton migration dynamics and includes the action of both spatially dependent depletion pulses (Fig. 2a), yielding a migration length of $L_d = 16 \pm 2$ nm (Supplementary Figs 6 and 7 and associated text). This migration length is defined for consistency with previous literature as $L_d = \sqrt{D\tau}$, for a diffusivity D (see Supplementary Text). This result is reproducible (Supplementary Fig. 8) and the measured migration length is independent of the excitation density (Supplementary Fig. 9), confirming that higher-order effects such as exciton–exciton annihilation do not contribute.

Modelling exciton migration

Having succeeded in obtaining a local measure of the extent of exciton migration, we turn to explaining the relatively long L_d for CN-PPV and its microscopic origin by employing Monte Carlo exciton hopping simulations[2,4,24,30–32] (see Supplementary Text). We employ an incoherent hopping model to obtain qualitative trends in the below-defined parameter space because we expect incoherent transport over the timescales of import in our measurements. By more generally identifying and relating parameters that impact exciton migration, we also hypothesize how other electronically coupled systems are situated within the same framework. Microscopically, we identify two distinct energetic considerations relevant to respectively determining the spatioenergetic landscape for migration and the way that excitons dynamically traverse it. First, a disordered organic solid is composed of closely spaced chromophore sites, where we define a site as the region over which an excitonic eigenstate is delocalized. The site transition energies are distributed due to variation in π-conjugation and configurations of moieties, interactions with neighbouring chromophores, and variation in the local electrostatic environment. This inhomogeneous site energy distribution, with characteristic width σ_{IH}, defines the spatioenergetic landscape for exciton migration (Supplementary Fig. 10). As important as defining this landscape for exciton migration is the energy scale that determines the way that the excitons are able to explore it. Therefore, we secondly consider the intrinsic excited-state configurational energy relaxation, or reorganization energy, of a chromophore, which determines the intramolecular Stokes shift, Δ, that we find dominates the dynamic character of migration over the spatioenergetic landscape (Supplementary Fig. 10). This intrinsic chromophore Stokes shift governs the typical exciton hop probability and duration by biasing excitations to hop downhill in energy and by limiting the spectral overlap for isoenergetic hops. In particular, whether exciton migration is diffusive or subdiffusive depends on the size of Δ relative to the total energy lost over the course of a migration trajectory, ΔE. The effects of each of σ_{IH} and Δ must, however, be considered relative to the intrinsic variation in a given chromophore's site energy, σ_{IT}. This intrinsic variation can be thought of as a generalized homogeneous broadening, occurring due to Franck–Condon progressions and fast thermal fluctuations, which for simplicity we take to be identical for each site. Since we find that σ_{IT} establishes an effective energy resolution for these two other contributors to respectively determine the spatioenergetic landscape and the nature of migration over the landscape, we plot and classify the average output parameters of the simulated trajectories as a function of the interchromophore variable σ_{IH}/σ_{IT}, the effective distinguishability of sites from one another, and the intrachromophore variable Δ/σ_{IT}, the strength of downhill bias for hopping within the inhomogeneous distribution.

By implementing this approach, we first determine the spatioenergetic landscape and corresponding nature of exciton migration that is most likely to underlie our $L_d \sim 16$ nm TRUSTED result in Fig. 2. We perform the Monte Carlo hopping simulations at multiple points in the σ_{IH}/σ_{IT}–Δ/σ_{IT} phase space (see Supplementary Text for details). We initiate each trajectory at the peak of a Gaussian inhomogeneous site energy distribution. Therefore, at long times the energy loss ΔE (Supplementary Fig. 11) over the course of a trajectory generally restricts the exciton to a slice of inhomogeneous site energy (and spatial) distribution with a diminished density of states relative to the initial condition[6,24,30]. We classify the nature of migration trajectories according to the power α that embodies the temporal evolution of their mean square displacement, MSD $\propto t^{\alpha}$. Although the use of a power law functional form is phenomenological, we find that it fits the simulation data well and with fewer parameters than a variety of other models whose diffusivities decay asymptotically to a finite value. We also find that it fits the data with less variability over the wide range of the σ_{IH}/σ_{IT}–Δ/σ_{IT} phase space that we explored (see Supplementary Fig. 12 and associated text). The deviation of α below unity signifies subdiffusive (sublinear with respect to time) mean square displacement. An example of both a linear and a

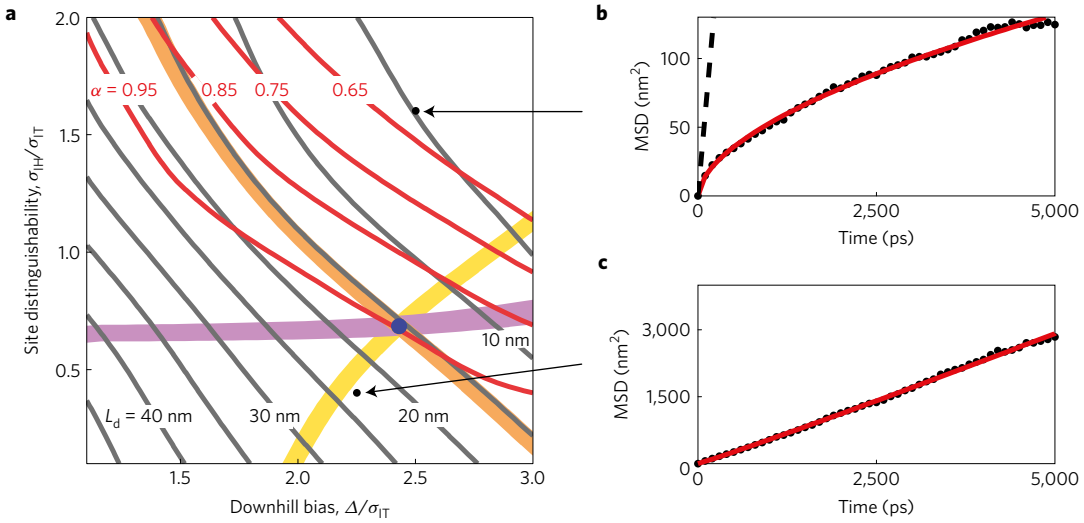

Figure 3 | Mapping the site distinguishability—downhill bias phase space to reveal the character of exciton migration. a, Monte Carlo exciton hopping simulation results plotted in the σ_{IH}/σ_{IT}–Δ/σ_{IT} phase space, where σ_{IH}/σ_{IT} represents the effective distinguishability of chromophore sites and where Δ/σ_{IT} represents the downhill hopping bias. Contours, obtained after averaging trajectories at each point in the phase space, for L_d are shown in grey; contours for α are shown in red. The location of the CN-PPV solid in the phase space is indicated with the blue dot. It is found by obtaining the intersection of the TRUSTED L_d result (orange contour), the contour for average trajectory energy loss relative to measured intrinsic Stokes shift (purple contour), and a contour obtained through the constraint on σ_{IH} and σ_{IT} imposed by the measured width of the absorption spectrum (yellow contour). The width of each of these three contours corresponds to a 1-σ uncertainty. **b**,**c**, Example mean square displacement (MSD) versus time for the two points indicated with arrows on the phase space in **a**. Data (black dots) is average of approximately 1,000 trajectories, and fit to determine α is shown in red. Although **c** shows diffusive (linear) behaviour for $\alpha = 1$, **b** corresponds to $\alpha = 0.62$. The dashed line represents a tangent to the slope at zero time to emphasize the extent of subdiffusivity. Note the stark difference in scales between **b** and **c**.

sublinear trajectory's mean square displacement illustrates the distinction between these behaviours (Fig. 3b,c). Averaging over many trajectories for a given point in the phase space enables us to map contour lines for the extent (L_d) and nature (α) of exciton migration. The resulting overlaid contour plots of L_d (grey) and α (red) are shown in Fig. 3a, and we analyse their behaviour in more detail when considering the general implications of this framework below.

Combining measurement and model

Presently, to identify the nature of exciton migration in CN-PPV we search in the same phase space for the intersection of the L_d result from our TRUSTED measurement (orange contour) and the average energetic relaxation over the exciton lifetime, ΔE, (spectral diffusion) obtained from the simulations, relative to the measured value of Δ (ref. 33) (purple contour, see also Supplementary Fig. 11). The intersection of these two curves also crosses the constraint (yellow contour) imposed by the width of the absorption spectrum (Fig. 1b), giving us further confidence in pinpointing CN-PPV at the location of the blue dot. Since this location in the phase space corresponds to $\alpha = 0.95$, we conclude that exciton migration in CN-PPV is essentially diffusive and that the large migration length of 16 nm results from the combination of diffusive migration with the long, 5-ns, fluorescence lifetime. Microscopically, the intrinsic broadening of the site energy is sufficient to make many sites energetically indistinguishable in spite of substantial inhomogeneous broadening, but is not sufficient to annul the downhill energy transfer bias imposed by a relatively large intrinsic Stokes shift. This Stokes shift is therefore likely to be the limiting factor in the extent of migration in CN-PPV solids.

Role of material energy scales in exciton migration

In addition to the particular analysis for CN-PPV, the constraints of our experiment and theoretical framework enable more general prediction of how the nature and extent of exciton migration vary as a function of the energy relationships that we have identified. The L_d contours in Fig. 3 roughly fall along the antidiagonal with the highest L_d values in the bottom left corner, where sites are essentially energetically indistinguishable. The α contours also roughly fall along the antidiagonal, with diffusive behaviour found in the bottom left and subdiffusive behaviour in the top right of the plot. In the limit of low site distinguishability and low downhill bias (bottom left) there are a high density of available sites for an exciton to hop to, and rapid hopping between them is possible, with little energy loss. This combination allows for extended diffusive migration ($\alpha = 1$). At the opposite extremes of high site distinguishability and large downhill hopping bias, each hop reduces the energy of the exciton and the density of available sites for subsequent hops. As a result, each hop takes longer than the previous one, and migration slows over the exciton lifetime ($\alpha < 1$). The migration length is also limited under these conditions because the exciton reaches an equilibrium energy within a narrow range of the inhomogeneous distribution that has a relatively low density of accessible sites, resulting in slow migration or even trapping[34]. Interpolating between the bottom left and top right of Fig. 3a, one can therefore rationalize that both L_d and α decrease along the diagonal of the plot. The roughly antidiagonal nature of their contours implies that the importance of site distinguishability and downhill bias can trade off to produce a similar resulting extent or nature of migration. Interestingly, however, a single L_d contour can intersect multiple values of α. That one can obtain the same overall extent of migration via hopping trajectories with different rates of energy loss implies that changes in the spatioenergetic landscape can be compensated by the manner in which it is traversed (Supplementary Fig. 13). As an overall prescription for long-range exciton hopping trajectories, one should seek to minimize the Stokes shift and inhomogeneous spectral linewidths of an electronically coupled material relative to the intrinsic site broadening. As a corollary, substantial intrinsic site broadening should be able to compensate for comparable site energy dispersity and reorganization energy.

Although the migration length values on Fig. 3 are specific to CN-PPV and we estimate an uncertainty in the Monte Carlo L_d values of ~20% (see Supplementary Figs 14–17 and associated text), these contours' trends should hold for other materials, modulated primarily in value by the fluorescence lifetime, chromophore density, oscillator strength, and any orientational anisotropies. We therefore hypothesize where other electronically coupled systems are situated within the above framework. Other conjugated polymer solids likely fall into a similar part of the generalized phase space as CN-PPV because substantial intrinsic site broadening is able to compensate the other energies in the problem. These other semiconductors generally suffer from shorter migration lengths (~5–20 nm) (refs 4,6,10–14), which we attribute primarily to their characteristically shorter fluorescence lifetimes, restricting the trajectory duration without compensating with faster hopping rates. In fact, given that the migration length depends not only on the fluorescence lifetime but also on this lifetime relative to the typical exciton hopping time, it is remarkable that CN-PPV's 25-fold increase in the lifetime over the canonical MEH-PPV translates only to a twofold increase in L_d (ref. 35). By contrast to conjugated polymer solids, nanocrystal arrays generally generate subdiffusive exciton trajectories located further from the phase space origin, albeit with longer migration lengths (tens of nm)[24]. We attribute this difference to the much longer nanocrystal excited-state lifetimes. In spite of their characteristically very narrow intrinsic linewidths that generate subdiffusion from polydispersity in size and energy, the slower hopping rates that accompany larger site spacings must still enable a compensating number of hops within the lifetime. In photosynthetic light harvesting, individual pigment–protein complexes can induce substantial energy relaxation, yet hopping between 'identical' protein complexes is paradoxically rapid (~ tens of ps)[7,8]. Here, having a hierarchy of intra- versus inter-protein interchromophore length and energy scales may illustrate a mechanism for high-efficiency exciton transport that is less well-captured by our hopping framework, even though inter-protein energy transfer is largely incoherent.

Although in the above analysis we localized conjugated polymer solids to a particular quadrant of the phase space in Fig. 3, we wish to make more specific predictions of what TRUSTED could reveal about the nature of exciton migration in other prominent conjugated polymer solids. Interestingly, despite their lower bandgaps that result in higher nonradiative rates and shorter exciton lifetimes, push–pull polymer materials are able to achieve high internal quantum efficiencies in photovoltaics[36–38]. Our TRUSTED approach could be used to determine the balance of exciton versus charge transport that underlies their high efficiencies. Furthermore, our experiments and analysis could dissect how the pseudo-charge transfer nature of their excited states, their large backbone dipole moments, and their substantial structural disorder affect the electronic energy landscape and resulting exciton migration properties. We anticipate that migration lengths would be shorter than in CN-PPV due to the difference in fluorescence lifetime but that intrinsic broadening might similarly be able to counterbalance the effects of disorder. The migration lengths would likely also be shorter in canonical amorphous polymer films such as in regio-random P3HT on account of its shorter lifetime. We hypothesize that TRUSTED could also reveal the combination of structural order, delocalization, and energetic broadening contributions that allow regio-regular P3HT to display an exciton diffusion length substantially longer than that of regio-random P3HT (ref. 39) and much more similar to that of CN-PPV. The fact that both partially ordered regio-regular P3HT and amorphous CN-PPV films support similar diffusion lengths highlights the complexity and multiplicity of material spatioenergetic landscape parameters that determine the observed diffusion length. Excitingly, TRUSTED should allow us to describe the combinations of the energy scales and morphologies that give rise to the diffusion lengths observed in different materials, even if these diffusion lengths appear similar due to different balances of competing contributions.

In sum, we have devised and executed an all-optical scheme to measure exciton migration within sub-diffraction excitation volumes on its native nanometre and picosecond scales. Through a combination of our measurements and simulations we determined that the disordered CN-PPV films that we interrogated exhibit a considerable exciton migration extent of ~16 nm in the diffusive regime, largely thanks to a relatively long fluorescence lifetime and to the intrinsic broadening of the chromophore site energy. In addition to our measurement and analysis of exciton migration in CN-PPV films, we developed a more general framework in which to contextualize our results by distinguishing between the inter- and intramolecular energy scales that influence the character and extent of exciton migration. We emphasize the significance of assessing inhomogeneous broadening and intrinsic chromophore Stokes shift effects on migration relative to intrinsic variations in chromophore site energies. As such, intrinsic site energy fluctuations are partially able to—or could be designed to—compensate for the latter effects in disordered electronically coupled molecular systems. For example, deliberately enhancing intrinsic chromophore energy fluctuations on molecular (or even material) scales by design could become an important strategy to extend exciton migration in photovoltaics, while suppressing it could prevent degradation in modern organic displays. We posit that the additional levels of multiscale hierarchy in photosynthetic light harvesting—namely intra- versus inter-protein exciton transfer and a potentially active protein scaffold with complementary physical properties to those of the pigment chromophores—could explain their exemplary transport efficiencies, which should be amenable to TRUSTED investigation in the future. Although the measured CN-PPV films appear, not surprisingly, to be amorphous on the scale of our measurement (Supplementary Fig. 18), TRUSTED is also inherently amenable to resolving spatial heterogeneity in exciton migration. Comparing migration heterogeneity maps to those of the physical heterogeneities observed in complex material microstructures should be a powerful approach to elucidate correlations between advantageous physical and functional intermolecular configurations in many electronically coupled molecular materials.

Methods

Methods, including statements of data availability and any associated accession codes and references, are available in the online version of this paper.

Received 30 October 2016; accepted 25 July 2017; published online 18 September 2017

References

1. Scholes, G. D. & Rumbles, G. Excitons in nanoscale systems. *Nat. Mater.* **5,** 683–696 (2006).
2. Brédas, J.-L., Beljonne, D., Coropceanu, V. & Cornil, J. Charge-transfer and energy-transfer processes in π-conjugated oligomers and polymers: a molecular picture. *Chem. Rev.* **104,** 4971–5004 (2004).
3. Scheblykin, I. G., Yartsev, A., Pullerits, T., Gulbinas, V. & Sundström, V. Excited state and charge photogeneration dynamics in conjugated polymers. *J. Phys. Chem. B* **111,** 6303–6321 (2007).
4. Menke, S. M. & Holmes, R. J. Exciton diffusion in organic photovoltaic cells. *Energy Environ. Sci.* **7,** 499–512 (2014).
5. Köhler, A. & Bässler, H. *Electronic Processes in Organic Semiconductors: An Introduction* (John Wiley, 2015).
6. Crooker, S. A., Hollingsworth, J. A., Tretiak, S. & Klimov, V. I. Spectrally resolved dynamics of energy transfer in quantum-dot assemblies: towards engineered energy flows in artificial materials. *Phys. Rev. Lett.* **89,** 186802 (2002).
7. Broess, K. *et al*. Excitation energy transfer and charge separation in photosystem II membranes revisited. *Biophys. J.* **91,** 3776–3786 (2006).

8. Bennett, D. I. G., Amarnath, K. & Fleming, G. R. A structure-based model of energy transfer reveals the principles of light harvesting in photosystem II supercomplexes. *J. Am. Chem. Soc.* **135,** 9164–9173 (2013).
9. Jailaubekov, A. E. *et al*. Hot charge-transfer excitons set the time limit for charge separation at donor/acceptor interfaces in organic photovoltaics. *Nat. Mater.* **12,** 66–73 (2013).
10. Mikhnenko, O. V., Blom, P. W. M. & Nguyen, T.-Q. Exciton diffusion in organic semiconductors. *Energy Environ. Sci.* **8,** 1867–1888 (2015).
11. Lin, J. D. A. *et al*. Systematic study of exciton diffusion length in organic semiconductors by six experimental methods. *Mater. Horiz.* **1,** 280–285 (2014).
12. Kozlov, O. V. *et al*. Real-time tracking of singlet exciton diffusion in organic semiconductors. *Phys. Rev. Lett.* **116,** 057402 (2016).
13. Gaab, K. M. & Bardeen, C. J. Anomalous exciton diffusion in the conjugated polymer MEH-PPV measured using a three-pulse pump–dump–probe anisotropy experiment. *J. Phys. Chem. A* **108,** 10801–10806 (2004).
14. Markov, D. E., Amsterdam, E., Blom, P. W. M., Sieval, A. B. & Hummelen, J. C. Accurate measurement of the exciton diffusion length in a conjugated polymer using a heterostructure with a side-chain cross-linked fullerene layer. *J. Phys. Chem. A* **109,** 5266–5274 (2005).
15. Lunt, R. R., Giebink, N. C., Belak, A. A., Benziger, J. B. & Forrest, S. R. Exciton diffusion lengths of organic semiconductor thin films measured by spectrally resolved photoluminescence quenching. *J. Appl. Phys.* **105,** 053711 (2009).
16. Groves, C., Reid, O. G. & Ginger, D. S. Heterogeneity in polymer solar cells: local morphology and performance in organic photovoltaics studied with scanning probe microscopy. *Acc. Chem. Res.* **43,** 612–620 (2010).
17. Clark, J., Silva, C., Friend, R. H. & Spano, F. C. Role of intermolecular coupling in the photophysics of disordered organic semiconductors: aggregate emission in regioregular polythiophene. *Phys. Rev. Lett.* **98,** 206406 (2007).
18. Noriega, R. *et al*. A general relationship between disorder, aggregation and charge transport in conjugated polymers. *Nat. Mater.* **12,** 1038–1044 (2013).
19. Liu, Y. *et al*. Aggregation and morphology control enables multiple cases of high-efficiency polymer solar cells. *Nat. Commun.* **5,** 5293 (2014).
20. Nguyen, T.-Q., Martini, I. B., Liu, J. & Schwartz, B. J. Controlling interchain interactions in conjugated polymers: the effects of chain morphology on exciton–exciton annihilation and aggregation in MEH–PPV films. *J. Phys. Chem. B* **104,** 237–255 (2000).
21. Wong, C. T. O., Lo, S. S. & Huang, L. Ultrafast spatial imaging of charge dynamics in heterogeneous polymer blends. *J. Phys. Chem. Lett.* **3,** 879–884 (2012).
22. Scully, S. R. & McGehee, M. D. Effects of optical interference and energy transfer on exciton diffusion length measurements in organic semiconductors. *J. Appl. Phys.* **100,** 034907 (2006).
23. Akselrod, G. M. *et al*. Visualization of exciton transport in ordered and disordered molecular solids. *Nat. Commun.* **5,** 3646 (2014).
24. Akselrod, G. M. *et al*. Subdiffusive exciton transport in quantum dot solids. *Nano Lett.* **14,** 3556–3562 (2014).
25. Penwell, S. B., Ginsberg, L. D. S. & Ginsberg, N. S. Bringing far-field subdiffraction optical imaging to electronically coupled optoelectronic molecular materials using their endogenous chromophores. *J. Phys. Chem. Lett.* **6,** 2767–2772 (2015).
26. Hell, S. W. & Wichmann, J. Breaking the diffraction resolution limit by stimulated emission: stimulated-emission-depletion fluorescence microscopy. *Opt. Lett.* **19,** 780–782 (1994).
27. Samuel, I. D. W., Rumbles, G. & Collison, C. J. Efficient interchain photoluminescence in a high-electron-affinity conjugated polymer. *Phys. Rev. B* **52,** R11573–R11576 (1995).
28. Buttafava, M., Boso, G., Ruggeri, A., Mora, A. D. & Tosi, A. Time-gated single-photon detection module with 110 ps transition time and up to 80 MHz repetition rate. *Rev. Sci. Instrum.* **85,** 083114 (2014).
29. Vicidomini, G. *et al*. Sharper low-power STED nanoscopy by time gating. *Nat. Methods* **8,** 571–573 (2011).
30. Lee, E. M. Y., Tisdale, W. A. & Willard, A. P. Can disorder enhance incoherent exciton diffusion? *J. Phys. Chem. B* **119,** 9501–9509 (2015).
31. Makhov, D. V. & Barford, W. Local exciton ground states in disordered polymers. *Phys. Rev. B* **81,** 165201 (2010).
32. Roberts, S. T. Energy transport: singlet to triplet and back again. *Nat. Chem.* **7,** 764–765 (2015).
33. Harrison, N. T. *et al*. Site-selective fluorescence studies of poly(p-phenylene vinylene) and its derivatives. *Phys. Rev. B* **53,** 15815–15822 (1996).
34. Hartenstein, B. & Bässler, H. Transport energy for hopping in a Gaussian density of states distribution. *J. Non-Cryst. Solids* **190,** 112–116 (1995).
35. Lewis, A. J. *et al*. Singlet exciton diffusion in MEH-PPV films studied by exciton–exciton annihilation. *Org. Electron.* **7,** 452–456 (2006).
36. Dimitrov, S. D. *et al*. Singlet exciton lifetimes in conjugated polymer films for organic solar cells. *Polymers* **8,** 14 (2016).
37. Rolczynski, B. S. *et al*. Ultrafast intramolecular exciton splitting dynamics in isolated low-band-gap polymers and their implications in photovoltaic materials design. *J. Am. Chem. Soc.* **134,** 4142–4152 (2012).
38. He, Z. *et al*. Single-junction polymer solar cells with high efficiency and photovoltage. *Nat. Photon.* **9,** 174–179 (2015).
39. Tamai, Y., Ohkita, H., Benten, H. & Ito, S. Exciton diffusion in conjugated polymers: from fundamental understanding to improvement in photovoltaic conversion efficiency. *J. Phys. Chem. Lett.* **6,** 3417–3428 (2015).

Acknowledgements

This work was supported by a David and Lucile Packard Fellowship for Science and Engineering to N.S.G., by The Dow Chemical Company under contract #244699, and by STROBE, A National Science Foundation Science and Technology Center under Grant No. DMR 1548924. Instrument development was supported by the Director, Office of Science, Chemical Sciences, Geosciences, and Biosciences Division, of the US Department of Energy under Contract No. DEAC02-05CH11231. We thank A. Tosi and M. Buttafava of SPAD lab, Politecnico di Milano, for discussions and the generous trial of the fast-gated SPAD and N. Bertone and PicoQuant GmbH for providing a demo of the HydraHarp400 photon counting apparatus. We thank D. M. Neumark for the use of a grating stretcher. S.B.P. acknowledges a Department of Energy Graduate Research Fellowship (contract no. DE-AC05-060R23100), R.N. thanks the Philomathia Foundation for postdoctoral support, and N.S.G. acknowledges an Alfred P. Sloan Research Fellowship and the Camille and Henry Dreyfus Teacher-Scholar Program.

Author contributions

S.B.P., L.D.S.G. and N.S.G. designed the research. S.B.P. and L.D.S.G. constructed the apparatus and performed the experiments. L.D.S.G. prepared the samples. S.B.P. performed and analysed the simulations. R.N. aided in the design and interpretation of the simulations. N.S.G. supervised the project. S.B.P. and N.S.G. wrote the manuscript and all authors revised and approved the manuscript.

Additional information

Supplementary information is available in the online version of the paper. Reprints and permissions information is available online at www.nature.com/reprints. Publisher's note: Springer Nature remains neutral with regard to jurisdictional claims in published maps and institutional affiliations. Correspondence and requests for materials should be addressed to N.S.G.

Competing financial interests

The authors declare no competing financial interests.

Methods

Sample preparation. Thin films of CN-PPV were prepared by spin-casting a ∼2.5 mg ml^{-1} solution of CN-PPV in chloroform on glass microscope coverslips in a nitrogen glove box, where they were encapsulated to protect them from oxygen during measurement. The solution was prepared by dissolving 9.8 mg CN-PPV in 1 ml chloroform and stirring on a hot plate overnight, then diluting 0.255 ml of this solution with 0.745 ml chloroform. The resulting solution was heated to 50° for ∼4 h before spin-casting at 8,000 r.p.m. for 1 min with an acceleration of 8,000 r.p.m. s^{-1}.

Characterization. A representative absorbance spectrum of a CN-PPV film was acquired with an ultraviolet–visible spectrophotometer (Agilent Cary 100). The fluorescence spectrum of CN-PPV solids was obtained with a Horiba Fluoromax-4 fluorimeter with 540 nm excitation wavelength and a 5 nm detection slit width.

Migration measurements. The TRUSTED scheme described above was employed in a home-built confocal microscope with a 63× 1.4NA Plan Apo Leica objective (HC PL APO 63×/1.40 oil CS2, Leica Material #11506350). The excitation and depletion laser pulse trains at 200 kHz were derived from third-harmonic and second-harmonic noncollinear optical parameteric amplifiers (NOPA) (Light Conversion), respectively, pumped by a 10 W Light Conversion PHAROS regeneratively amplified laser system with a fundamental wavelength of 1,030 nm. The 3-fJ excitation pulse was centred at 540 nm, and the two 240-pJ depletion pulses were centred at 740 nm with a bandwidth set to 14 nm. The depletion pulses were produced, with a variable relative delay, by splitting the initial pulse with a polarization beam splitting cube and directing one pulse though an optical delay stage (Newport ILS-250-CC) before recombining the pulses with a second polarization beam splitting cube. Both the pump and depletion pulses were fibre coupled into single-mode polarization-maintaining fibres to produce high-quality Gaussian modes. A vortex phase mask (RPC Photonics VPP-1a) was then used to generate the annular depletion pulse beam mode. The pulses were then directed into the microscope with dichroic mirrors (Chroma T650spxr and T600lpxr-UF2) through a quarter waveplate positioned to circularly polarize the depletion pulses. During the experiment, the sample is rastered with a PI Nano scanning piezoelectric stage (P-545.3C7) in steps of 30 μm over a 60 μm × 60 μm area. Data from the resulting nine spatial locations can be averaged to improve the signal-to-noise ratio or analysed separately. Epifluorescence is collected between 635 and 640 nm through dichroic mirrors and emission filters (two ET625/30m and one ET640/10m from Chroma) and is focused onto a fast-gated SPAD detector with a 200-ps rise time (A. Tosi, SPAD lab, Politecnico di Milano; PicoQuant) controlled by a Picosecond Delayer (MPD) that is triggered just after the arrival of the second depletion pulse to eliminate fluorescence occurring before the definition of the detection volume. We phase lock the detection data stream to the timing of an optical chopper (Newport 3501) placed in the excitation pulse line, so that we may separately determine the photon count rates during the 'excitation on' and 'excitation off' chopper phases for multiple cycles. The count rates obtained during these open and closed phases of the chopper are each corrected for the classic pile-up effect with a simple Poisson correction factor (see Supplementary Information) before we take the difference of the two to isolate the count rate that is attributed to the modulated excitation pulse only. The second depletion pulse is separately modulated with a shutter so that data collected when this pulse is blocked can be used as a reference and control. The signal versus delay time obtained when this second depletion pulse is unblocked is divided by the signal versus delay time observed when it is blocked. The resulting data is then normalized to the extrapolated value of this ratio at zero delay time to calculate the fraction of remaining excitations in the detection volume as a function of the delay time (see Supplementary Information for more details).

Fitting methods. The length scale of exciton migration was extracted from the experimental data using a custom fitting function. The fitting function is a simplified model of the experiment, which employs diffusive expansion of the exciton distribution between its creation and detection. It explicitly includes the action of the modes of all three light pulses in the experiment (see Supplementary Information for details). The fit parameter is the diffusivity, D, which is then used to calculate the migration length, $L_d = \sqrt{D\tau}$. The uncertainty in the migration length is then found through a combination of the uncertainty in the diffusivity from the fit, which accounts for the error in the data and the quality of the fit, and the uncertainty in the resolution of the microscope, which is an input parameter for the fit (see Supplementary Information for details).

Monte Carlo simulations. Simulations of incoherent exciton hopping trajectories were performed with discrete hops on an 80 nm × 80 nm 2D hexagonal lattice with periodic boundary conditions and a density of 1.4 sites nm^{-2}. For each trajectory, site energies were randomly assigned in accordance with the assumed Gaussian inhomogeneous broadening width, and trajectories were initiated at the average energy (peak of the inhomogeneous distribution). Hopping rates between pairs of sites were then calculated from the site energies, the site-to-site separation, the intrinsic spectral width of the sites, and the intrinsic Stokes shift, in a combined Dexter and FRET transfer model (see Supplementary Information for details). Approximately 1,000 trajectories were averaged for each set of parameters and the resulting mean squared displacement over time was fitted to a power law model to extract the migration length and characteristic power, α.

Data availability. The datasets generated during and/or analysed during the current study are available from the corresponding author on reasonable request.